Local magnetic cluster size identified by neutron total scattering in the site-diluted spin glass $Sn_xFe_{4-x}N$ ($x = 0.88$)

Yuanpeng Zhang,[1,2] Tanja Scholz,[3,4] Richard Dronskowski,[3,*] Marshall T. McDonnell,[1] and Matthew G. Tucker[1,†]

[1]*Neutron Scattering Division, Oak Ridge National Laboratory (ORNL), Oak Ridge, Tennessee 37830, USA*

[2]*Materials Measurement Science Division, National Institute of Standards and Technology (NIST), 100 Bureau Drive, Gaithersburg, Maryland 20899, USA*

[3]*Institute of Inorganic Chemistry, RWTH Aachen University, 52056 Aachen, Germany*

[4]*Nanochemistry Department, Max Planck Institute for Solid State Research, Heisenberstrasse 1, Stuttgart 70569, Germany*

(Received 1 November 2018; revised manuscript received 3 February 2019; published 16 July 2019)

A detailed structure analysis for the site-diluted $Sn_xFe_{4-x}N$ ($x = 0.25$, 0.41, and 0.88) has been carried out through complex modeling of the neutron total scattering data. We present quantitative evidence showing the local ferromagnetic cluster size extending to ~8 Å on average when $Sn_{0.88}Fe_{3.12}N$ undergoes the spin-glass transition (the other two not showing such a transition). The modeling methodology used in this work involving the corefinement of the nuclear and magnetic structure in both real and reciprocal space can potentially be applied generally to explore a variety of spin-glass material problems.

DOI: 10.1103/PhysRevB.100.014419

I. INTRODUCTION

Starting in the 1970s, there has been research into theoretically describing the unusual properties (e.g., susceptibility, specific heat, electrical resistivity, etc.) of spin-glass materials using the cluster approach [1–7]. To this aim, the spin cluster size is an important concern and there have been various experimental approaches for characterizing the cluster size, or local correlation length. A commonly used approach is to measure the temperature dependence of AC susceptibility with different frequency and amplitude variations, where the cluster size can be estimated by the change in the cusp position with frequency following the Vogel-Fulcher law [8–16]. Other approaches for identifying the cluster spin glass and revealing the local correlation length include nuclear magnetic resonance [17–19], inelastic neutron scattering [19–26], and Mössbauer spectroscopy [27–32]. Here we provide an alternative approach using neutron total scattering. Through modeling the data, a direct picture of the local magnetic ordering in real space can be established [33] and the cluster spin glass can then be inspected, quantitatively. In contrast to Bragg diffraction which focuses on the long-range order of crystalline system, the total scattering includes both Bragg peaks and diffuse scattering. Through Fourier transform, the corresponding real-space pair distribution function (PDF) pattern can provide information focusing on the local ordering even in the absence of long-range crystalline structure [34,35]. Therefore, with the neutron total scattering data fitted in both real and reciprocal space, the structure (nuclear and magnetic) extending from local to medium range can be covered. Concerning the magnetic ordering, such local-to-medium range information can be utilized to provide an estimation for the spin-glass cluster size. In fact, neutron total scattering has been used as a powerful tool to examine the local magnetic ordering for frustrated or spin-freezing systems [36–38]. Here, we first focus on the nuclear-only PDF pattern (with magnetic contribution carefully removed), providing a quantitative characterization of the site-dilution. Then the nuclear and magnetic corefinement for the neutron total scattering data is presented. By defining a local magnetic order parameter, we were able to inspect the spin-glass clustering quantitatively.

II. METHODOLOGY

The phase-pure, polycrystalline $Sn_xFe_{4-x}N$ used in this study were synthesized by a two-step ammonolytic reaction starting from the powdered reactants Sn and Fe_2O_3 that were mixed and finely ground using various ratios of the metal atoms (refer to Ref. [39] for a detailed synthesis description). According to our previous report, the samples with $x = 0.25$, 0.41 do not show spin-glass transition, and the sample with $x = 0.88$ does show the spin-glass transition at 12 K [40]. Here, the x values were obtained from Rietveld refinement, according to our previous report. The neutron total scattering data were measured on the NOMAD time of flight diffractometer at Spallation Neutron Source, ORNL, and the measurements were taken at 300, 100, and 10 K, respectively for all three samples. The 300 and 100 K data were collected for 1 h at each point in the cryostream sample environment and the 10 K data were collected for 2 h in a cryostat. Both the Rietveld-like refinement (with DiffPy-CMI [41]) and supercell-based reverse Monte Carlo (RMC) modeling (with RMCProfile [42]) were used for the data analysis. A conceptual diagram demonstrating such a comprehensive analysis approach employing neutron total scattering is presented in Fig. 1. Here it should be mentioned that the magnetic

*Corresponding author: drons@HAL9000.ac.rwth-aachen.de
†tuckermg@ornl.gov

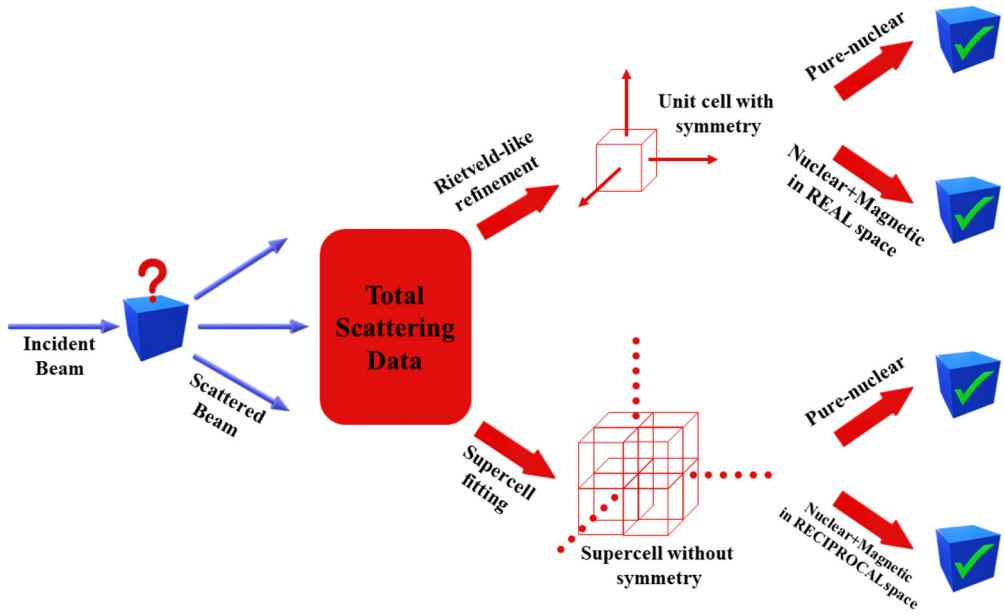

FIG. 1. The conceptual diagram showing the two different approaches for modeling the total scattering data. Apart from the pure-nuclear Rietveld refinement, all the other three approaches are used in the paper. Here short names are given for the four approaches, UN, UNM, SN, and SNM, where U represents unit-cell, S is for supercell, N is for nuclear, and M is for magnetic.

scattering is implemented in real and reciprocal space, respectively, in DiffPy-CMI and RMCProfile.

III. NUCLEAR STRUCTURE ANALYSIS

Before the corefinement, we first focus on the pure-nuclear PDF [supercell nuclear (SN) approach, the RMCProfile $D(r)$ function is used in this paper. Refer to the report by Keen [43] for terminology of various PDF functions] data using RMCProfile with the magnetic signal excluded (technical details can be found in the supplemental material [44]). The fitting result of the pure-nuclear PDF is shown in Fig. 2 for the 10 K dataset (results for 100 K and 300 K datasets are shown in Fig. S1 and Fig. S2) with the corresponding R factor (refer to Fig. 2 for the definition) presented for each sample. Using the obtained structure configuration, we calculated the local correlation coefficients (LCCs) with respect to various distance window for all the three samples. The mathematical formulation defining the local correlation coefficient is given as [44]

$$P_{ij}(D_{\min}, D_{\max}) = \frac{1}{N_i + N_j} \sum_{k}^{N_i} \frac{1}{N_{\text{shell}}} \sum_{l}^{N_j} f(k,l), \quad (1)$$

where

$$f(k,l) = \begin{cases} 1, \text{ if } D_{\min} \leqslant \|\overrightarrow{r_k} - \overrightarrow{r_l}\| \leqslant D_{\max} \\ 0, \text{ otherwise.} \end{cases} \quad (2)$$

With such notations, the inner summation represents the number of atoms of type j within a certain shell surrounding the k^{th} atom of type i. The normalization factor N_{shell} is the total number of type-i and type-j atoms contained in the corresponding shell. N_i and N_j then refer to the total number of atoms with type i and j, respectively.

From its definition, the LCC concerns only the static nuclear structure. Therefore, we ignore its temperature dependence and picked one temperature point as a representative. Here the 10-K data is used for all three samples.

As shown in the inset of Fig. 3(a), there are two crystallographic sites for the Fe atoms in the γ'-Fe_4N lattice, and it was previously shown that the substitution takes place on the $1a$ Wykoff site with the $3c$ site fully occupied by Fe [39,40].

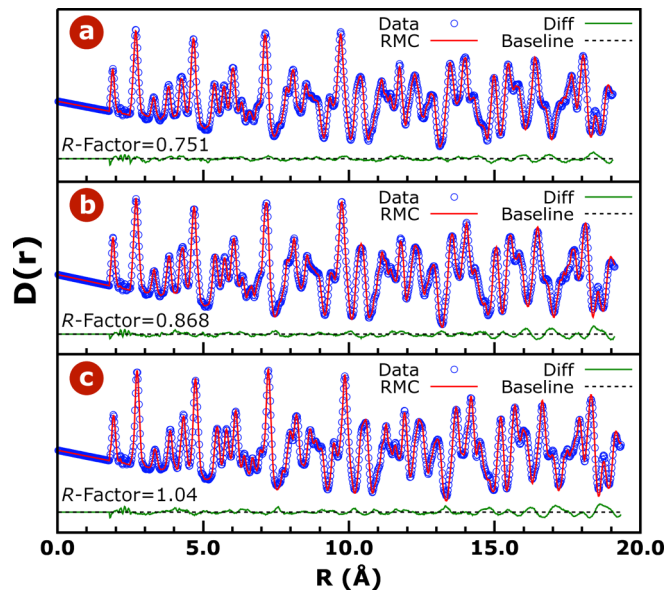

FIG. 2. The PDF fitting with SN approach using RMCProfile for (a) $Sn_{0.25}Fe_{3.75}N$, (b) $Sn_{0.41}Fe_{3.59}N$, and (c) $Sn_{0.88}Fe_{3.12}N$, respectively, at 10 K. The R factor given in the figure is defined as follows:$R = \sum_i (y_{C,i} - y_{O,i})^2 / \sum_i y_{O,i}^2$, where y_C and y_O represents the calculated and observed value, respectively. The same definition applies across the whole article.

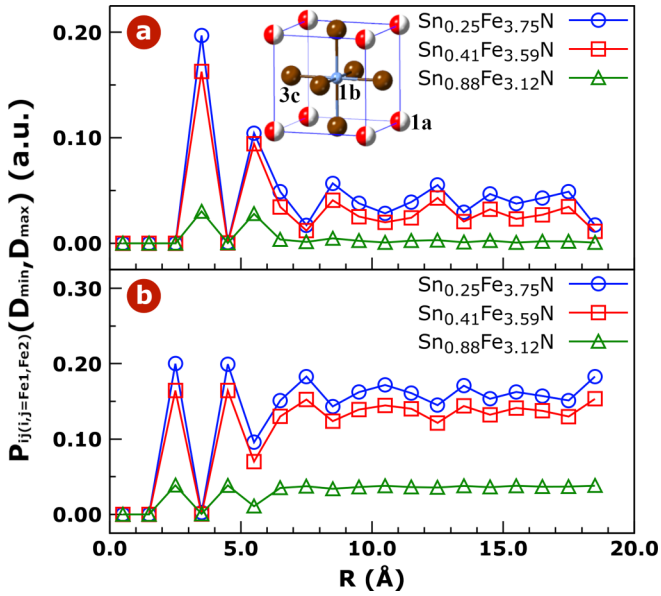

FIG. 3. The local correlation coefficients for (a) Fe1–Fe1 and (b) Fe1–Fe2 pairs, with respect to various distance windows. Here R is defined as the center of the distance window: $R = (D_{\min} + D_{\max})/2$. The inset of (a) shows the unit cell of $Sn_xFe_{4-x}N$ with the antiperovskite crystal structure in space group $pm\bar{3}m$. The body center ($1b$) is occupied by N. The face center ($3c$) is fully occupied by Fe, and the substitution occurs only on the $1a$ position according to Refs. [39,40].

Here the iron atoms sitting on the $1a$ and $3c$ sites are denoted as Fe1 and Fe2, respectively. The LCCs for the pairs involving Fe1 atoms (i.e., Fe1-Fe1 and Fe1-Fe2 pairs) are then shown in Fig. 3. By comparing across the three samples, one can observe that the LCC of $Sn_{0.88}Fe_{3.12}N$ (which shows the spin-glass state) is significantly reduced as compared to $Sn_{0.25}Fe_{3.75}N$ and $Sn_{0.41}Fe_{3.59}N$ across the whole distance window range. Considering the LCC [refer to Eq. (1)] has already been normalized, the low LCC corresponding to the distance window from local to medium range is an intrinsic property of the sample due to the site dilution effect. From another perspective, the LCC can be regarded as an indicator for randomness of the magnetic site occupation [45], which is one of the crucial ingredients for the spin-glass state transition.

IV. MAGNETIC STRUCTURE ANALYSIS

Next, we focus on the magnetic structure of the three samples, using the Rietveld-like refinement for the PDF data. Here the nuclear and magnetic PDF data are corefined [thereby the unit-cell nuclear magnetic (UNM) approach], by employing the magnetic PDF (mPDF) functionality [46] implemented in the DiffPy-CMI framework. The refinement result for the data measured at 10 K is presented in Fig. 4. The 100 and 300 K datasets, together with the extracted lattice parameters, are shown in Figs. S10–Fig. S12 in the supplemental material [44]. From Figs. 4(a) to 4(c), one can observe a good quality of the corefinement for each of the samples. Furthermore, by subtracting the pure nuclear contribution from the raw PDF data, the magnetic PDF is obtained, which is shown in Fig. 4(d) together with the refinement result. Here, the magnetic PDF can only be clearly observed (considering the noise level of the data) within the region bounded with the green-dashed line (1.6–6.0 Å) as indicated in Fig. 4(d). Therefore, only this region is considered for the refinement, with the calculated value for all the points beyond that region set to zero. The interesting aspect is that the magnetic PDFs for all the three samples are quite similar and do not distinguish the spin-glass state sample, $Sn_{0.88}Fe_{3.12}N$. To inspect

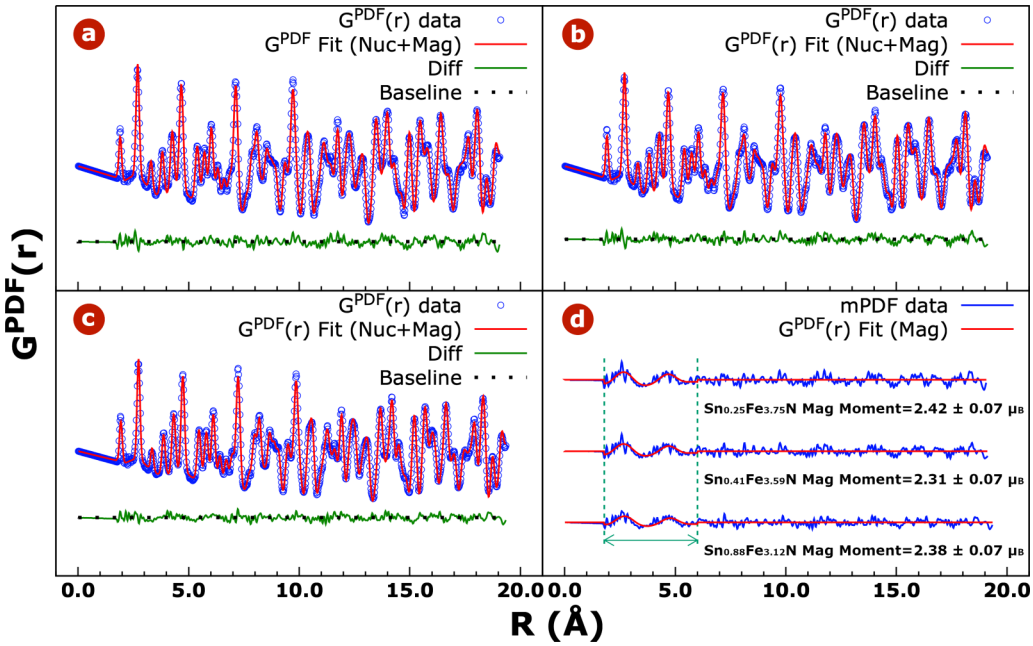

FIG. 4. The PDF refinement (following the UNM approach) result for (a) $Sn_{0.25}Fe_{3.75}N$, (b) $Sn_{0.41}Fe_{3.59}N$, and (c) $Sn_{0.88}Fe_{3.12}N$ data (at 10 K), respectively. In (d), the magnetic PDF is presented for all samples with the extracted magnetic moments labeled out for each. The green-dashed line and arrow indicate the region of interest for the magnetic PDF refinement.

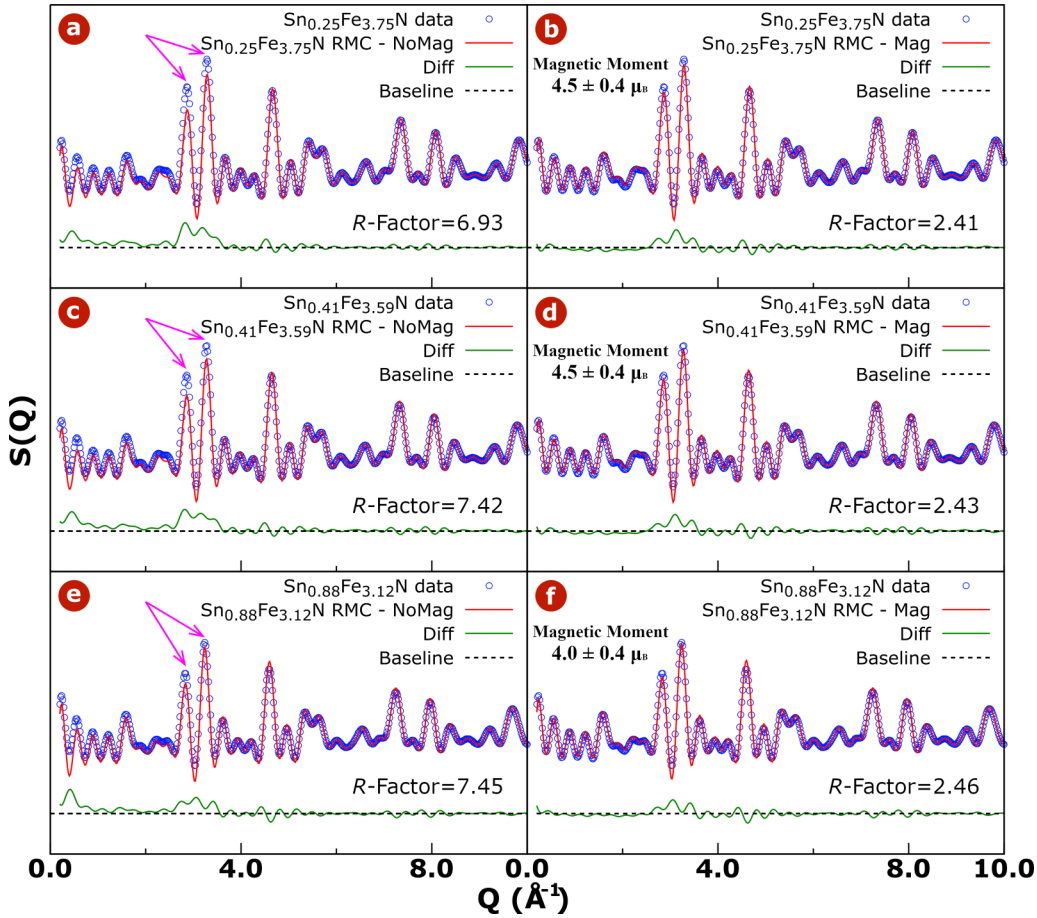

FIG. 5. The result of the RMCProfile modeling for the $S(Q)$ data. (a), (c), and (e) are the pure nuclear modeling without considering the magnetic contribution, for $Sn_{0.25}Fe_{3.75}N$, $Sn_{0.41}Fe_{3.59}N$ and $Sn_{0.88}Fe_{3.12}N$, respectively. (b), (d), and (f) are the result when magnetic scattering is taken into account, corresponding to (a), (c), and (e), respectively.

the result quantitatively, the magnetic moments are extracted from the refined parameters using the following formulation [47,48]:

$$S_{\text{fit}} = \sqrt{\frac{gB\langle b\rangle^2}{An_s}} S_{\text{norm}}, \tag{3}$$

where A (dimensionless) and B (with a dimension of L^{-2}, refer to the supplemental material [44] for details) are the nuclear and magnetic PDF scale factor, respectively. $\langle b\rangle$ refers to the average nuclear scattering length, n_s is the fraction of the magnetic atoms and g is the Landé factor (here the value of 2 is used, assuming pure spins without orbital contributions). S_{norm} then is the norm of the moment specified internally for the magnetic species, and here the two different types of Fe atoms are treated to be the same (i.e., with the same norm of the magnetic moment) for the magnetic PDF refinement. The extracted average magnetic moment for each sample is shown in Fig. 4(d) alongside the corresponding refinement result. The similar magnitude of the moment concerning the local magnetic order for all the three samples then infers that even though the $Sn_{0.88}Fe_{3.12}N$ is in a spin-glass state, locally the ferromagnetic (FM) ordering persists up to ~6 Å.

Although the total scattering data presented in the real and reciprocal spaces are mathematically just the Fourier transform pairs, they reflect different aspects of the examined structure; the real-space PDF emphasizes the local ordering and the reciprocal pattern emphasizes the long-range ordering, or average structure. To further examine the clustering in the spin-glass state, we inspect the total scattering data in reciprocal space. Again, RMCProfile modeling is used, including the magnetic contribution to the reciprocal space pattern [therefore, the supercell nuclear magnetic (SNM) approach here, for more technical details about the modeling, refer to the supplemental material [44]. Also, refer to the report by Keen [43] for terminology of the Q-space total scattering functions]. First, the fitting with only the nuclear contribution taken into account is shown in Figs. 5(a), 5(c), and 5(e) for the 10-K datasets. Here, one can see clear discrepancies between the RMCProfile modeling and the experimental data, especially in the low-Q region where the magnetic signal mainly resides owing to the strongly Q-dependent magnetic form factor. The result for 100 and 300 K datasets can be found in Figs. S22–S25 in the supplemental material [44], where no such clear discrepancy can be observed even without considering the magnetic contribution to the calculated $S(Q)$.

According to our previous results [39,40], $Sn_xFe_{4-x}N$ is ferromagnetic in the magnetically ordered region before undergoing the spin-glass transition. Here, it should be noted that the principle of magnetic-nuclear corefinement for the

neutron total scattering data is that the two contributions can be decoupled. In other words, when one does the pure-nuclear refinement, the remainder beyond the noise level can then be attributed to the magnetic contribution. For the 100 and 300 K datasets, the $S(Q)$ pattern can be fully rebuilt through structural distortion. Therefore, in such situations, the magnetic and nuclear contributions cannot be decoupled due to the relatively stronger thermal effect (as compared to the 10-K datasets). In comparison, the extra features around 3 $Å^{-1}$ in the 10 K datasets are beyond the level of thermal effect. Therefore, those features should come from the magnetic contribution. In other words, for the 10-K datasets, the magnetic and nuclear contributions can be decoupled, considering the fact that the magnetic moments for samples at 10 K is larger than that for 100 and 300 K situations.

Focusing on the 10-K dataset, the experiment-modeling discrepancy concerning the two main magnetic Bragg peaks [indicated by the magenta arrows in Figs. 5(a), 5(c), and 5(e) is more significant for $Sn_{0.25}Fe_{3.75}N$ and $Sn_{0.41}Fe_{3.59}N$ (nonspin glass) than that for $Sn_{0.88}Fe_{3.12}N$ (spin glass). This result clearly infers the loss of the long-range magnetic ordering for the $Sn_{0.88}Fe_{3.12}N$ spin-glass sample. Once the magnetic contribution is taken into account, better agreement is obtained for all the three temperature points across the whole Q range, as can be observed in Figs. 5(b), 5(d), and 5(f). Here for clarity of presentation, only the region below 10 $Å^{-1}$ is shown, and the corresponding plot for the Q range beyond 10 $Å^{-1}$ can be found in Fig. S21. For the magnetic contribution, the magnetic form factor of Fe^{2+} (Fe1 atom) and Fe^{1+} (Fe2 atom) was used [49] and the magnetic moments of Fe1 and Fe2 atoms are assumed to be the same (see the supplemental material [44] for more information). The reason why the same magnetic moment but different magnetic form factor was used is that the magnetic moment behaves simply as a Q-independent scale factor in the magnetic scattering calculation. Therefore, an average value for both Fe1 and Fe2 atoms was used. However, the magnetic form factor is strongly Q dependent, and the dependence for Fe1 and Fe2 is quite different (see Ref. [49]). Therefore, the magnetic form factor for Fe1 and Fe2 atoms should be treated differently. Furthermore, larger magnetic moments for both Fe1 and Fe2 atoms were used, as compared to those obtained from the Rietveld-like refinement [see Fig. 4(d)] – 4.5 μ_B for $Sn_{0.25}Fe_{3.75}N$ and $Sn_{0.41}Fe_{3.59}N$, 4.0 μ_B for $Sn_{0.88}Fe_{3.12}N$. Here unlike the Rietveld-like refinement, the supercell-based fitting of the total scattering data relies on absolute scaling of the data. Therefore, in principle there should not be any scale factor during the refinement. However, since the nuclear and magnetic scattering is convolved in the Q-space data, it is challenging to separate out the magnetic scattering signal on an absolute scale with RMCProfile. Therefore, a reasonable value of the magnetic moments to be used in the RMCProfile modeling has to be obtained through trial and error. What we found is that only when using the values given above can we get an overall reasonable agreement with the experimental $S(Q)$ data, especially concerning the two main magnetic scattering Bragg peaks (refer to the magenta arrows in Fig. 5). For example, the results with the several trials of magnetic moments are presented in Figs. S13–S15, from which one can clearly observe a worse fit for the two magnetic Bragg peaks, as compared to the results shown in Fig. 5. Quantitatively, we changed the magnetic moments used for the refinement and uncertainty of the magnetic moment values could be estimated based on the criterion that the fitting quality is not changed significantly. With the allowance of the R-factor changing set to be 5%, the estimated uncertainty of the magnetic moments is $\sim 0.4\,\mu_B$.

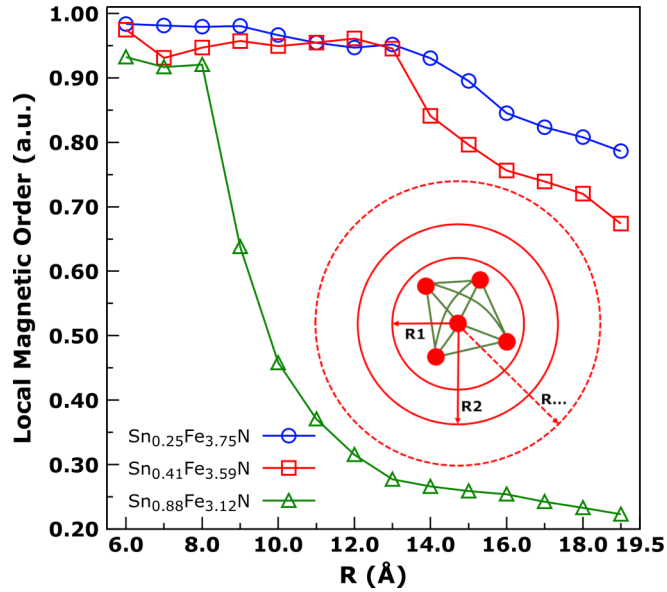

FIG. 6. The average LMOP across all local clusters with various cluster radius for all three samples.

For further quantitative discussion, we carried out magnetic clustering analysis. First, one specifies a certain cluster radius (e.g., 6 Å). Then each single Fe atom in the system is taken as the center atom, respectively, and the corresponding local cluster is built up. All the Fe atoms (including the center atom itself) with distance from the center atom smaller than the prespecified cluster radius are included in the local cluster. For each Fe atom pair, the dot product of the magnetic moment vectors ($\vec{S}_i$ for the i^{th} Fe atom), called the local magnetic order parameter (LMOP), is used to determine the ferromagnetic/antiferromagnetic (FM/AFM) property for that pair. Mathematically, the LMOP is defined as

$$\text{LMOP}_{ij} = \frac{\vec{S}_i \cdot \vec{S}_j}{\| \vec{S}_i \| \| \vec{S}_j \|}. \tag{4}$$

Then, the LMOP of the cluster is calculated by first summing up the LMOPs for all possible Fe atom pairs and then averaging over the total number of pairs within the cluster, as illustrated in the inset of Fig. 6. Furthermore, for each cluster size, a single LMOP is obtained by averaging over all the local clusters with the specified radius, and the result is presented in Fig. 6. For $Sn_{0.25}Fe_{3.75}N$ and $Sn_{0.41}Fe_{3.59}N$, the LMOP stays at a level close to 1, which indicates the FM characteristics are well maintained locally (or even to a medium-range). For the spin-glass $Sn_{0.88}Fe_{3.12}N$ sample, an FM feature can still be observed locally when the cluster size is below ~8 Å. Beyond that, the LMOP suddenly drops as can be observed clearly in Fig. 6. Quantitatively, it shows that for $Sn_{0.88}Fe_{3.12}N$, the

local FM correlation is well maintained till the cluster size reaches ∼8 Å. Here the local cluster size obtained from fitting the $S(Q)$ data is larger than that (∼6 Å) obtained from the mPDF anlaysis. Concerning such a discrepancy, it should be pointed out that the determination of the upper limit for mPDF (where the signal extends to) is based on an arbitrary selection. As aforementioned, the reason for this is the low signal-to-noise level around and beyond 6 Å. In contrast, the spin cluster size is determined in a systematic way based on the model obtained from fitting the $S(Q)$ data. Therefore, in the latter approach, one can observe an obvious falling off of the calculated LMOP parameter beyond 8 Å.

V. SUMMARY

In summary, a complex modeling scheme has been used to identify critical ingredients for spin-glass state formation. Owing to the substitution on the magnetic sites, the local correlation coefficient of the magnetic species is significantly reduced. Furthermore, through modeling the magnetic total scattering in both real and reciprocal space, local FM cluster is identified for the $Sn_{0.88}Fe_{3.12}N$ sample in the spin-glass state, with a cluster size of ∼8 Å on average. We believe revealing such correlation length should benefit the theoretical description for the spin-glass systems. For example, it could provide guidance for the cluster size control when simulating spin-glass systems following the three-dimensional Edward-Anderson model [3]. Also, it is worth pointing out that the comprehensive methodologies used in this report could be applied extensively in probing both the nuclear and magnetic structure of spin-glass systems in a general sense.

ACKNOWLEDGMENTS

The research at ORNL's Spallation Neutron Source was sponsored by the Scientific User Facilities Division, Office of Basic Energy Sciences, US Department of Energy (DOE). The financial support by Deutsche Forschungsgemeinschaft and RWTH Graduiertenförderung (scholarship to T. Scholz) is gratefully acknowledged. We also want to thank Dr. Benjamin Frandsen for the help on the nuclear and magnetic PDF corefinement with the DiffPy-CMI framework.

This work has been partially supported by UT-Battelle, LLC, under Contract No. DE-AC05-00OR22725 with the US Department of Energy. The United States Government retains and the publisher, by accepting the article for publication, acknowledges that the United States Government retains a nonexclusive, paid-up, irrevocable, worldwide license to publish or reproduce the published form of this manuscript, or allow others to do so, for United States Government purposes. The DOE will provide public access to these results of federally sponsored research in accordance with the DOE Public Access Plan (http://energy.gov/downloads/doepublic-access-plan).

[1] K. Binder, Z. Phys. B Condens. Matter **26**, 339 (1977).
[2] J. Houdayer, Eur. Phys. J. B **22**, 479 (2001).
[3] T. Jorg, Progr. Theor. Exp. Phys. **157**, 349 (2005).
[4] S. J. Poon and J. Durand, Phys. Rev. B **18**, 6253 (1978).
[5] O. Redner, J. Machta, and L. F. Chayes, Phys. Rev. E **58**, 2749 (1998).
[6] C. M. Soukoulis and K. Levin, Phys. Rev. Lett. **39**, 581 (1977).
[7] R. H. Swendsen and J. S. Wang, Phys. Rev. Lett. **58**, 86 (1987).
[8] P. Bag, P. R. Baral, and R. Nath, Phys. Rev. B **98**, 144436 (2018).
[9] T. Chakrabarty, A. V. Mahajan, and S. Kundu, J. Phys.: Condens. Matter **26**, 405601 (2014).
[10] A. Kumar, R. P. Tandon, and V. P. S. Awana, J. Appl. Phys. **110**, 043926 (2011).
[11] A. Aharoni, Phys. Lett. A **99**, 458 (1983).
[12] V. K. Anand, D. T. Adroja, and A. D. Hillier, Phys. Rev. B **85**, 014418 (2012).
[13] H. Khurshid, P. Lampen-Kelley, O. Iglesias, J. Alonso, M. H. Phan, C. J. Sun, M. L. Saboungi, and H. Srikanth, Sci. Rep. **5**, 15054 (2015).
[14] A. Kumar, R. P. Tandon, and V. P. S. Awana, Eur. Phys. J. B **85**, 238 (2012).
[15] V. Kumar, R. Kumar, K. Singh, S. K. Arora, I. V. Shvets, and R. Kumar, J. Appl. Phys. **116**, 073903 (2014).
[16] S. Shtrikman and E. P. Wohlfarth, Phys. Lett. A **85**, 467 (1981).
[17] A. P. Dioguardi *et al.*, Phys. Rev. Lett. **111**, 207201 (2013).
[18] A. K. Grover, L. C. Gupta, R. Vijayaraghavan, M. Matsumura, M. Nakano, and K. Asayama, Solid State Commun. **30**, 457 (1979).
[19] X. Y. Lu *et al.*, Phys. Rev. B **90**, 024509 (2014).
[20] T. E. Mason, in *Handbook on the Physics and Chemistry of Rare Earths* (Elsevier, Amsterdam, 2001), p. 281.
[21] V. K. Anand, D. T. Adroja, A. D. Hillier, J. Taylor, and G. Andre, Phys. Rev. B **84**, 064440 (2011).
[22] S. M. Gaw, E. C. Andrade, M. Vojta, C. D. Frost, D. T. Adroja, D. Prabhakaran, and A. T. Boothroyd, Phys. Rev. B **88**, 165121 (2013).
[23] A. Krimmel, H. Mutka, M. M. Koza, V. Tsurkan, and A. Loidl, Phys. Rev. B **79**, 134406 (2009).
[24] K. Motoya, Pramana J. Phys. **63**, 155 (2004).
[25] T. J. Sato, H. Takakura, A. P. Tsai, and K. Shibata, Phys. Rev. B **73**, 054417 (2006).
[26] R. S. Solanki, S. H. Hsieh, C. H. Du, G. Deng, C. W. Wang, J. S. Gardner, H. Tonomoto, T. Kimura, and W. F. Pong, Phys. Rev. B **95**, 024425 (2017).
[27] J. Burghaus, M. T. Sougrati, A. Mochel, A. Houben, R. P. Hermann, and R. Dronskowski, J. Solid State Chem. **184**, 2315 (2011).
[28] J. K. Srivastava, S. Ramakrishnan, A. K. Nigam, G. Chandra, R. Vijayaraghavan, V. Srinivas, J. Hammann, G. Jehanno, and J. P. Sanchez, Hyperfine Interact. **42**, 1079 (1988).
[29] W. T. Herrera, Y. T. Xing, S. M. Ramos, P. Munayco, M. B. Fontes, E. M. Baggio-Saitovitch, and F. J. Litterst, Phys. Rev. B **84**, 014430 (2011).
[30] A. Ito, S. Morimoto, and K. Iwai, Il Nuovo Cimento D **18**, 263 (1996).
[31] L. Kalinowski, M. Kądziołka-Gaweł, and A. Ślebarski, Phys. Rev. B **98**, 245140 (2018).

[32] S. N. Mishra, V. Balasubramanian, S. D'Souja, D. Rambabu, R. G. Pillay, A. K. Grover, and P. N. Tandon, Hyperfine Interact. **34**, 519 (1987).
[33] A. M. P. Joseph, J. R. Stewart, and L. G. Andrew, J. Phys.: Condens. Matter **25**, 454220 (2013).
[34] T. D. Martin, *Structure and Dynamics: An Atomic View of Materials* (Oxford University Press, Oxford, 2003).
[35] V. M. Nield and D. A. Keen, *Diffuse Neutron Scattering from Crystalline Materials* (Oxford University Press, Oxford, 2001).
[36] J. A. M. Paddison, M. Daum, Z. Dun, G. Ehlers, Y. Liu, Matthew B. Stone, H. Zhou, and M. Mourigal, Nat. Phys. **13**, 117 (2016).
[37] J. A. M. Paddison, H. Jacobsen, O. A. Petrenko, M. T. Fernández-Díaz, P. P. Deen, and A. L. Goodwin, Science **350**, 179 (2015).
[38] J. A. M. Paddison and A. L. Goodwin, Phys. Rev. Lett. **108**, 017204 (2012).
[39] T. Scholz and R. Dronskowski, Inorg. Chem. **54**, 8800 (2015).
[40] T. Scholz and R. Dronskowski, AIP Adv. **6**, 055107 (2016).
[41] P. Juhas, C. Farrow, X. Yang, K. Knox, and S. Billinge, Acta Crystallogr. A **71**, 562 (2015).
[42] G. T. Matthew, A. K. David, T. D. Martin, L. G. Andrew, and H. Qun, J. Phys. Condens. Matter **19**, 335218 (2007).
[43] D. A. Keen, J. Appl. Crystallogr. **34**, 172 (2001).
[44] See Supplemental Material at http://link.aps.org/supplemental/10.1103/PhysRevB.100.014419 for results and technical details of the neutron total scattering data fitting following UNM, SN, and SNM approaches as described in the main text.
[45] A. V. Ceguerra, M. P. Moody, R. C. Powles, T. C. Petersen, R. K. W. Marceau, and S. P. Ringer, Acta Crystallogr. A **68**, 547 (2012).
[46] B. A. Frandsen, X. Yang, and S. J. L. Billinge, Acta Crystallogr. A **70**, 3 (2014).
[47] K. Kodama, K. Ikeda, S. Shamoto, and T. Otomo, J. Phys. Soc. Jpn. **86**, 124708 (2017).
[48] A. Benjamin and J. L. Simon, Acta Crystallogr. A **71**, 325 (2015).
[49] A. J. Freeman and J. P. Desclaux, J. Magn. Magn. Mater. **12**, 11 (1979).